

Burgers dynamics for Poisson point process initial conditions of the Weibull class

Patrick Valageas¹

¹*Université Paris-Saclay, CEA, CNRS, Institut de Physique théorique, 91191 Gif-sur-Yvette, France*

We derive the statistical properties of one-dimensional Burgers dynamics with stochastic initial conditions for the velocity potential defined by a Poisson point process whose intensity follows a power law with exponent $\alpha > -1$. Working in the inviscid limit and exploiting the geometrical construction of solutions in terms of first-contact parabolas, we derive explicit analytical expressions for a broad set of statistical quantities. These include the one- and two-point probability distributions of the velocity, the multiplicity functions of voids and shocks, and the velocity and density correlation functions together with their associated power spectra. We also show that the full hierarchy of n -point distributions factorizes into a sequence of two-point conditional probabilities. This class of initial conditions leads to self-similar evolution and produces probability distributions characterized by stretched-exponential tails, with tail exponents spanning the full range from unity to infinity. The associated characteristic length scale grows as a power law of time, with an exponent lying between zero and one half.

I. INTRODUCTION

Nonlinear transport phenomena driven by advection and dissipation play a fundamental role in statistical physics. A classic model in this context is the Burgers equation [1–3], which provides a minimal framework where nonlinear steepening and dissipative effects both appear. In the inviscid regime—where the viscosity ν tends toward zero—velocity gradients grow increasingly sharp until shock discontinuities develop [1, 4, 5], separated by linear velocity ramps. The resulting fields display strong intermittency and highly nonuniform density patterns. Consequently, Burgers turbulence serves as an important theoretical setting for studying nonlinear stochastic processes in far-from-equilibrium environments [6, 7], with applications ranging from turbulence phenomenology [8, 9] to irreversible aggregation models [10, 11].

In this work, we investigate the deterministic Burgers equation without any external noise, so that randomness arises solely from stochastic initial conditions. This deterministic inviscid Burgers equation also appears in cosmology, as the so-called "adhesion model" [12–15] to model the formation of large-scale structures. The infinitesimal viscosity halts shell crossings and avoids the unphysical particle escape from potential wells entailed by the simpler Zeldovich approximation [16, 17].

A significant portion of prior work considers Gaussian initial conditions with power-law spectra [4, 18, 19]. These lead to self-similar evolutions with an expanding integral scale. Although the Hopf–Cole transformation [2, 3] gives an explicit expression for the solution at arbitrary time in terms of the initial state, closed-form statistical results are only available in special cases—for instance, for Brownian initial velocity fields [20, 21] or for white-noise initial velocities [22, 23].

Another class of initial conditions that yields explicit results is based on Poisson point processes. When the Poisson intensity follows a power law, the dynamics again become self-similar. Building on [24, 25], we recently studied the case of negative exponents $\alpha < -3/2$ [26], which leads to Fréchet-type probability distributions with heavy power-law tails. In this paper, following [27, 28], we instead focus on exponents $\alpha > -1$, which produce Weibull-type distributions characterized by stretched-exponential tails. We extend previous analyses by computing one- and two-point statistics of both the velocity and density fields for arbitrary Poisson exponent α , and by providing numerical results for representative examples.

This paper is organized as follows. In Section II, we review the equations of motion, the geometric interpretation of the system, and the class of initial conditions considered, and we show two numerical realizations illustrating the dependence on the exponent α . Section III derives the one-point Eulerian velocity distribution $P_0(v)$. In Section IV, we present the two-point Eulerian distributions of the velocity and density fields, along with the void distribution and the energy power spectrum. Higher-order distributions are briefly discussed in Section V. In Section VI, we turn to the Lagrangian statistics of particle displacements and derive the shock multiplicity function. We conclude in Section VII.

II. EQUATIONS OF MOTION AND INITIAL CONDITIONS

A. Equations of motion

We consider in this article the one-dimensional Burgers equation [1] for the velocity field $v(x, t)$ in the limit of vanishing viscosity,

$$\frac{\partial v}{\partial t} + v \frac{\partial v}{\partial x} = \nu \frac{\partial^2 v}{\partial x^2} \quad \text{with} \quad \nu \rightarrow 0^+, \quad (1)$$

together with the associated density field $\rho(x, t)$, which satisfies the continuity equation for an initially uniform density ρ_0 [29]. As is well known [2, 3, 13], introducing the velocity potential $\psi(x, t)$ defined by $v = \partial\psi/\partial x$, and applying the transformation $\psi(x, t) = -2\nu \ln \theta(x, t)$, reduces the Burgers equation to the linear heat equation for θ . This yields the explicit solution

$$v(x, t) = \frac{\partial \psi}{\partial x} \quad \text{with} \quad \psi(x, t) = -2\nu \ln \int_{-\infty}^{\infty} \frac{dq}{\sqrt{4\pi\nu t}} \exp \left[-\frac{(x-q)^2}{4\nu t} - \frac{\psi_0(q)}{2\nu} \right], \quad (2)$$

where $\psi_0(q) = \psi(q, t=0)$ is the initial potential. In the limit $\nu \rightarrow 0^+$, the steepest-descent method gives [7, 13]

$$\psi(x, t) = \min_q \left[\psi_0(q) + \frac{(x-q)^2}{2t} \right] \quad \text{and} \quad v(x, t) = \frac{x - q(x, t)}{t}, \quad (3)$$

where the Lagrangian coordinate $q(x, t)$ denotes the point at which the minimum is achieved. Eulerian positions x for which the minimization problem admits two solutions, $q_- < q_+$, correspond to shock locations, and all mass initially between q_- and q_+ collapses to the point x . The mapping $q \mapsto x(q, t)$ is known as the Lagrangian map, whereas its inverse $x \mapsto q(x, t)$ is the inverse Lagrangian map. They are discontinuous at the locations of voids and shocks [7, 14].

B. Geometrical interpretation and Legendre transform

As is well known [1, 13], the minimization problem in Eq.(3) has a simple geometrical interpretation. Consider the downward-opening parabola $\mathcal{P}_{x,c}(q)$ centered at x and of maximum value c , defined by

$$\mathcal{P}_{x,c}(q) = c - \frac{(q-x)^2}{2t}. \quad (4)$$

Starting from a very negative value of c , so that the parabola lies entirely below $\psi_0(q)$, we increase c until the parabola first touches the initial potential. The abscissa of this point of first contact gives the Lagrangian coordinate $q(x, t)$ and the corresponding potential is $\psi(x, t) = c$.

The expression (3) for the velocity potential can also be written using a Legendre-Fenchel transform [14, 15, 18]. Define the linear Lagrangian potential $\varphi_L(q, t)$ and the associated Lagrangian map $x_L(q, t)$ by

$$\varphi_L(q, t) = \frac{q^2}{2} + t\psi_0(q), \quad x_L(q, t) = \frac{\partial \varphi_L}{\partial q} = q + tv_0(q), \quad (5)$$

which describe the evolution in the absence of shocks. Introducing

$$H(x, t) = \frac{x^2}{2} - t\psi(x, t), \quad (6)$$

the minimization in Eq.(3) becomes

$$H(x, t) = \max_q [xq - \varphi_L(q, t)] = \mathcal{L}_x[\varphi_L(q, t)], \quad (7)$$

where \mathcal{L}_x denotes the Legendre transform evaluated at x . In this way, $\psi(x, t)$ is obtained from $\psi_0(q)$ through a Legendre transform, which simultaneously yields the inverse Lagrangian map $q(x, t)$ and the velocity field $v(x, t)$.

C. Initial condition

In this paper, following [27], we consider stochastic initial conditions for $\psi_0(q)$ generated by a Poisson point process with intensity $\lambda(\psi_0)$ in the upper half-plane ($q, \psi_0 > 0$). Thus, the initial state consists of a set of points $\{(q, \psi_0)_i\}$, and the probability of finding n points within any domain \mathcal{B} is given by the Poisson law

$$P(N_{\mathcal{B}} = n) = \frac{\Lambda(\mathcal{B})^n}{n!} e^{-\Lambda(\mathcal{B})}, \quad \text{with} \quad \Lambda(\mathcal{B}) = \int_{\mathcal{B}} dq d\psi_0 \lambda(\psi_0). \quad (8)$$

As in [27], we focus on the case where the intensity $\lambda(\psi_0)$ follows a power-law,

$$\psi_0 > 0: \quad \lambda(\psi_0) = a \psi_0^\alpha, \quad a > 0, \quad \alpha > -1, \quad \text{and for } \psi_0 \leq 0: \quad \lambda(\psi_0) = 0. \quad (9)$$

The condition $\alpha > -1$ ensures that $\Lambda(\mathcal{B}_{x,c})$ is finite when $\mathcal{B}_{x,c}$ denotes the region below the parabola $\mathcal{P}_{x,c}(q)$ defined in Eq.(4), with $c > 0$. In what follows, we study the velocity and density fields obtained from Eq.(3) for the power-law intensity (9). Because $\lambda(\psi_0)$ is independent of q , the system remains statistically homogeneous at all times.

This Poisson point process gives a discrete set of points $\{(q, \psi_0)_i\}$. Although this does not define a continuous initial velocity potential $\psi_0(q)$, one may formally construct such a function by drawing, from each point $\{(q, \psi_0)_i\}$, two nearly vertical line segments with slopes $\pm\gamma$ extending upward to infinity, and then connecting the resulting narrow triangular regions. For a finite number of points within a bounded interval $[q_1, q_2]$, and upon restricting to points with $\psi_{0,i} \leq \psi_{\max}$, this procedure yields a continuous function $\psi_0(q)$. Then, in the limits $\gamma \rightarrow \infty$ and $\psi_{\max} \rightarrow \infty$, these auxiliary vertical segments become irrelevant, as the first-contact parabolas defined in Eq.(4) intersect only the original lower summits $\{(q, \psi_0)_i\}$. However, thanks to the geometrical construction in Eqs.(3)-(4), this intermediate regularization is unnecessary. The minimization in Eq.(3) can be taken directly over the discrete set of points $\{(q, \psi_0)_i\}$, which fully determines the evolved potential $\psi(x, t)$ for all times $t > 0$. One could as well define the initial condition by this potential computed at a time $t_i > 0$.

D. Self-similar dynamics

We introduce the rescaled coordinates

$$x = a^{-1/(2\alpha+3)} t^{(\alpha+1)/(2\alpha+3)} X, \quad v = a^{-1/(2\alpha+3)} t^{-(\alpha+2)/(2\alpha+3)} V, \quad \psi = a^{-2/(2\alpha+3)} t^{-1/(2\alpha+3)} \Psi. \quad (10)$$

The initial potential ψ_0 is rescaled in the same way to Ψ_0 , for any given time t . This yields, at all times,

$$\Psi(X, t) = \min_i \left[\Psi_{0,i} + \frac{(X - Q_i)^2}{2} \right] \quad \text{and} \quad V(X, t) = X - Q_{i_*}, \quad (11)$$

where i_* denotes the Poisson point for which the minimum is attained. The intensity measure of the Poisson process becomes

$$\Lambda(\mathcal{B}) = \int_{\mathcal{B}} dQ d\Psi_0 \lambda(\Psi_0) \quad \text{with} \quad \lambda(\Psi_0) = \Psi_0^\alpha \text{ for } \Psi_0 > 0, \quad \lambda(\Psi_0) = 0 \text{ for } \Psi_0 \leq 0. \quad (12)$$

Because this rescaling removes all explicit dependence on time, the dynamics are statistically self-similar for all $t > 0$. In particular, the integral length scale $L(t)$ —defined, for instance, as the scale separating the large- and small-scale asymptotic regimes—grows with time as

$$L(t) \propto t^\gamma \quad \text{with} \quad \gamma = \frac{\alpha + 1}{2\alpha + 3}, \quad 0 < \gamma < \frac{1}{2}. \quad (13)$$

Thus, $L(t)$ always grows more slowly than \sqrt{t} , the limit attained as $\alpha \rightarrow \infty$. The normalization constant a is also absorbed by the rescaling (10), so the dynamics depend only on the exponent α . In the following, we focus on equal-time statistics and therefore work exclusively with the rescaled variables (10), using lowercase letters for simplicity.

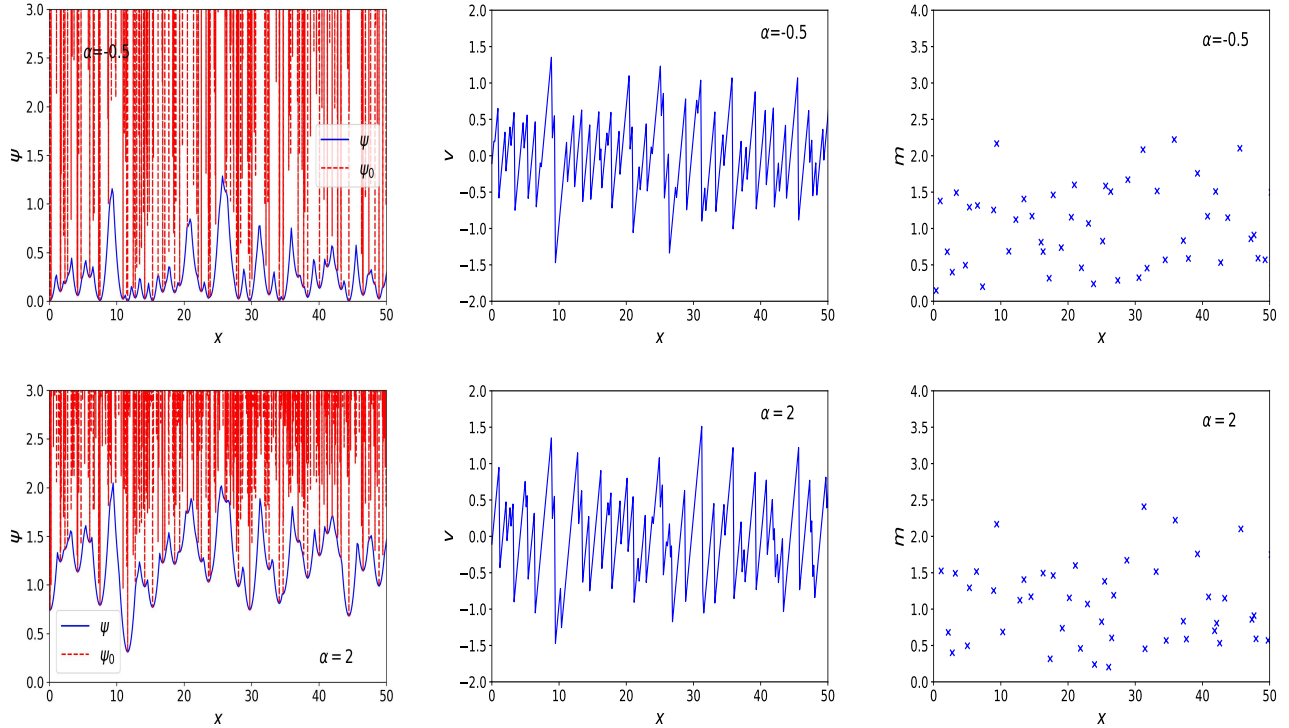


Figure 1. A realization of the system for the cases $\alpha = -1/2$ (top row) and $\alpha = 2$ (bottom row) at time $t = 1$. *Left column*: the initial velocity potential $\psi_0(x)$ (red dashed curve) and the evolved velocity potential $\psi(x, t)$ (blue solid curve). *Middle column*: velocity field $v(x, t)$. *Right column*: mass and location of the shocks.

E. Numerical realizations

Figure 1 shows numerical realizations of the system for two representative cases, $\alpha = -0.5$ (top row) and $\alpha = 2$ (bottom row). We use the rescaled coordinates (10), which also correspond to the choice $t = 1$ and $a = 1$. The initial potential $\psi_0(q)$ is generated directly from a random number routine, using the fact that the Poisson point process (9) becomes homogeneous in the (q, y) plane under the change of variable $y = \psi_0^{\alpha+1}/(\alpha + 1)$. The potential $\psi(x, t)$ and velocity $v(x, t)$ at time t are then obtained through the Legendre transform (7).

The initial velocity potential ψ_0 is highly singular, being defined by a Poisson point process. We show in the figure the upward vertical lines originating from the points $\{(q, \psi_0)_i\}$, following the construction described in Section II C. The evolved potential $\psi(x, t)$ consists of a family of upward parabolic arcs, as predicted by Eq.(3), with their minima located at the deepest minima of ψ_0 . For the larger value of α the potential ψ becomes more narrowly concentrated around $\psi \simeq 1$.

The velocity field $v(x, t)$ displays the characteristic linear ramps x/t of Burgers dynamics, separated by shocks corresponding to downward jumps. The visual appearance of the velocity field, as well as the shock positions x_s and their masses $m_s = \Delta q$ (marked by the crosses in the right panels), is similar for both values of α . This is because the key statistical properties of the system—such as the void distribution and the shock multiplicity function—exhibit comparable behaviors and differ mainly in the exponent of their stretched-exponential tails. These rare-event tails are difficult to discern by eye, and the most apparent feature in Fig. 1, common to all α , is the steep decay of the probability distributions, which confines most fluctuations to a finite range. This stands in contrast with the Fréchet-type initial conditions studied in [26], which produce heavy power-law tails that are easily visible and distinguishable in such plots.

In the following Sections, we derive analytical expressions for the probability distributions of displacement, velocity, and density fields, as well as the statistics of voids and shocks associated with these dynamics.

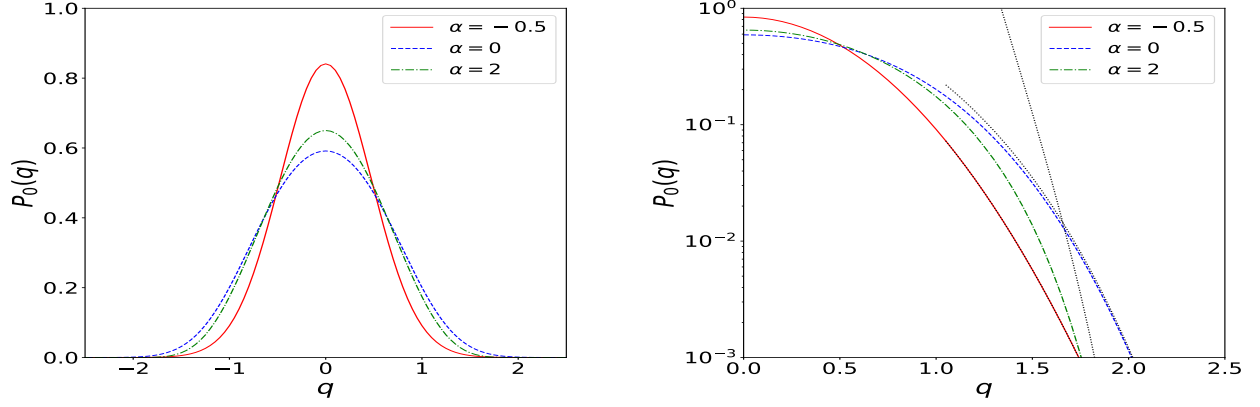


Figure 2. One-point probability distribution $P_0(q) = P_0(v)$ of the Lagrangian coordinate q , or of the velocity v , from Eq.(16). We display our results on a linear scale (left panel) and a logarithmic scale (right panel), for the cases $\alpha = -0.5, 0$, and 2 . The dotted lines in the right panel are the asymptotic results (18).

F. Limit $\alpha \rightarrow \infty$

In the limit $\alpha \rightarrow \infty$, the Poisson intensity (12) implies that very few points lie below $\Psi_0 = 1$, while many lie above. Consequently, the first-contact parabolas have $c \simeq 1$, a trend already visible in the realizations for $\alpha = -0.5$ and 2 shown in Fig. 1. On the other hand, from Eq.(38) below, the number of voids per unit length grows as $\sqrt{\alpha}$, indicating that the typical length scale decreases as $1/\sqrt{\alpha}$. Therefore, in this limit, it is natural to rescale lengths, velocities and potentials as

$$q = \tilde{q}/\sqrt{\alpha}, \quad x = \tilde{x}/\sqrt{\alpha}, \quad v = \tilde{v}/\sqrt{\alpha}, \quad \psi = 1 + \tilde{\psi}/\alpha. \quad (14)$$

One can explicitly check that by substituting these rescaled variables into the results derived in the following Sections, one indeed obtains finite probability distributions. Moreover, these expressions coincide with the $\alpha \rightarrow \infty$ limit obtained in [26] for Fréchet-class initial conditions (corresponding to $\alpha \rightarrow -\infty$ in the notation of Eq.(9)). In addition, they also match the late-time results obtained for Gaussian initial conditions with vanishing large-scale power [4, 9, 13], $E_0(k) \propto k^n$ with $n > 1$ [19], or in the hyperbolic asymptotic scaling [30]. By considering the Poisson point process (9) for the initial potential itself, we generalize this regime to the full class $\alpha > -1$, producing stretched-exponential tails that vary with α . Furthermore, it is no longer necessary to focus on a late-time asymptotic regime, since the dynamics are now fully self-similar. However, whereas the stretched-exponential tails such as (18) have an exponent that diverges for $\alpha \rightarrow \infty$, the rescaling (14) yields Gaussian tails in the limit $\alpha \rightarrow \infty$. The explicit expressions obtained in this limit can be found in [26], so we do not consider it further in this article.

III. ONE-POINT EULERIAN DISTRIBUTIONS

In this Section, we consider the one-point probability distribution $P_x(q)$ of the Lagrangian coordinate q corresponding to a given Eulerian position x . This also provides the distribution of the velocity, $P_x(v)$, with $v = x - q$. Owing to the statistical translational invariance, it is sufficient to focus on $x = 0$, since $P_x(q)$ depends only on $|q - x|$, so that $P_x(q) = P_0(|q - x|)$. Then, the probability $P_0(q, c)dqdc$ that the first-contact point occurs at Lagrangian coordinate q with parabola height c reads

$$P_0(q, c) = \lambda(c - q^2/2) e^{-\Lambda_\alpha c^{\alpha+3/2}} \quad \text{with} \quad \Lambda_\alpha = \frac{\sqrt{2\pi}\Gamma(\alpha+1)}{\Gamma(\alpha+5/2)}. \quad (15)$$

This gives for the probability distribution $P_0(q)$

$$P_0(q) = \int_{q^2/2}^{\infty} dc (c - q^2/2)^\alpha e^{-\Lambda_\alpha c^{\alpha+3/2}}. \quad (16)$$

This distribution is even in q , it has a finite value at the origin,

$$P_0(q=0) = \frac{1}{\alpha+1} \Lambda_\alpha^{-(2\alpha+2)/(2\alpha+3)} \Gamma\left(\frac{4\alpha+5}{2\alpha+3}\right), \quad (17)$$

and a stretched-exponential tail at large distance

$$q \gg 1 : \quad P_0(q) \simeq \Gamma(\alpha+1) \left((2\alpha+3) \Lambda_\alpha 2^{-\alpha-3/2} q^{2\alpha+1} \right)^{-\alpha-1} e^{-\Lambda_\alpha 2^{-\alpha-3/2} q^{2\alpha+3}}. \quad (18)$$

Since for $x = 0$ we have $v = -q$, the velocity probability distribution $P_0(v) = P_0(q = -v)$ is given by the same expression. In the cases $\alpha = -1/2$ and 0 the integral (16) reads

$$\alpha = -1/2 : \quad L(t) \propto t^{1/4}, \quad P_0(q) = 2^{-1/4} e^{-\pi q^2/\sqrt{2}}, \quad (19)$$

$$\alpha = 0 : \quad L(t) \propto t^{1/3}, \quad P_0(q) = 2^{-2/3} 3^{-1/3} \Gamma\left(\frac{2}{3}, \frac{2q^3}{3}\right). \quad (20)$$

Figure 2 shows the curves $P_0(q)$ for the cases $\alpha = -0.5, 0$, and 2 . These same values of α will also be used in the subsequent figures throughout this article. We verify that our numerical evaluation of Eq.(16) is consistent with the asymptotic stretched-exponential tail given in (18). As already observed in the sample realizations shown in Fig. 1, the velocity distribution is qualitatively similar for different values of α . It is mainly characterized by a bell-shaped peak at $v = 0$, followed by a monotonic decrease for $|v| > 0$ and a sharp cutoff of order unity. The dependence on α is most visible in the exponent of the stretched-exponential tail, which affects only the extreme, rare-event part of the distribution and has little impact on the bulk statistics. The same pattern will be encountered for the other statistical quantities studied in the following Sections. This behavior contrasts with that of Poisson initial conditions in the Fréchet class studied in [26], corresponding to $\alpha < -3/2$ in Eq.(9), which lead to heavy power-law tails and therefore produce a much stronger dependence of the dynamics on the exponent α .

IV. TWO-POINT EULERIAN DISTRIBUTIONS

A. Two first-contact parabolas

In this Section we consider two-point Eulerian probability distributions, such as $P_{x_1, x_2}(q_1, q_2)$, the probability that the Eulerian positions x_1 and x_2 map to the Lagrangian coordinates q_1 and q_2 . As in Section III, we first examine the probability $P_{x_1, x_2}(q_1, c_1; q_2, c_2)$ that the first-contact points lie at q_1 and q_2 , with parabola heights c_1 and c_2 . For the Poisson point process (12), this is

$$\begin{aligned} x_1 < x_2 : \quad P_{x_1, x_2}(q_1, c_1; q_2, c_2) = & \left[\frac{\lambda(\psi_\star)}{x_2 - x_1} \delta_D(q_1 - q_\star) \delta_D(q_2 - q_\star) + \theta(q_1 < q_\star) \theta(q_2 > q_\star) \lambda(c_1 + (q_1 - x_1)^2/2) \right. \\ & \left. \times \lambda(c_2 + (q_2 - x_2)^2/2) \right] e^{-\int_{-\infty}^{q_\star} dq \int_0^{c_1 - (q - x_1)^2/2} d\psi \lambda(\psi) - \int_{q_\star}^{\infty} dq \int_0^{c_2 - (q - x_2)^2/2} d\psi \lambda(\psi)}, \end{aligned} \quad (21)$$

where δ_D and θ denote the Dirac delta distribution and Heaviside function, and (q_\star, ψ_\star) is the intersection of the two parabolas:

$$q_\star = \frac{x_1 + x_2}{2} + \frac{c_1 - c_2}{x_2 - x_1}, \quad \psi_\star = c_1 - \frac{(q_\star - x_1)^2}{2} = c_2 - \frac{(q_\star - x_2)^2}{2} = \frac{c_1 + c_2}{2} - \frac{(x_2 - x_1)^2}{8} - \frac{(c_2 - c_1)^2}{2(x_2 - x_1)^2}. \quad (22)$$

For $q < q_\star$, the parabola \mathcal{P}_{x_1, c_1} lies above \mathcal{P}_{x_2, c_2} , while for $q > q_\star$ the opposite holds, since we take $x_1 < x_2$. The first term in the bracket corresponds to the case where both parabolas share a common first-contact point with the initial potential $\psi_0(q)$, which is also their intersection (q_\star, ψ_\star) . The second term corresponds to the case where the two first-contact points q_1 and q_2 are distinct, with $q_1 < q_\star < q_2$. We now introduce the change of variables

$$\bar{x} = \frac{x_1 + x_2}{2}, \quad x = x_2 - x_1 > 0, \quad q_1 = \bar{x} + q'_1, \quad q_2 = \bar{x} + q'_2, \quad (23)$$

integrate over (c_1, c_2) , and transform the integration variables from (c_1, c_2) to (q'_\star, ψ_\star) . This yields

$$P_x(q'_1, q'_2) = \int_{-\infty}^{\infty} dq'_\star \int_{\psi_{\min}(q'_\star)}^{\infty} d\psi_\star \left[\lambda(\psi_\star) \delta_D(q'_1 - q'_\star) \delta_D(q'_2 - q'_\star) + x \theta(q'_1 < q'_\star) \theta(q'_2 > q'_\star) \psi_- (q'_1)^\alpha \psi_+ (q'_2)^\alpha \right] e^{-\mathcal{I}}, \quad (24)$$

with

$$\begin{aligned}\psi_-(q') &= \max \left[0, \psi_* + \frac{1}{2} \left(q'_* + \frac{x}{2} \right)^2 - \frac{1}{2} \left(q' + \frac{x}{2} \right)^2 \right], \quad \psi_+(q') = \max \left[0, \psi_* + \frac{1}{2} \left(q'_* - \frac{x}{2} \right)^2 - \frac{1}{2} \left(q' - \frac{x}{2} \right)^2 \right], \\ \mathcal{I}(\psi_*, q'_*) &= \frac{1}{\alpha + 1} \left[\int_{-\infty}^{q'_*} dq' \psi_-(q')^{\alpha+1} + \int_{q'_*}^{\infty} dq' \psi_+(q')^{\alpha+1} \right],\end{aligned}\tag{25}$$

and

$$|q'_*| \geq \frac{x}{2} : \quad \psi_{\min}(q'_*) = 0, \quad |q'_*| < \frac{x}{2} : \quad \psi_{\min}(q'_*) = -\frac{1}{2} \left(|q'_*| - \frac{x}{2} \right)^2.\tag{26}$$

The minimum ψ_{\min} enforces the conditions that the parabola heights c_1 and c_2 remain positive and that the upper portions of the parabolas \mathcal{P}_1 and \mathcal{P}_2 are not entirely below one another, ensuring that each has a non-vanishing interval of admissible first-contact points. For the first term in Eq.(24), the factor $\lambda(\psi_*)$ actually implies $\psi_* > 0$, since this configuration requires a Poisson point at the intersection (q_*, ψ_*) . This expression shows explicitly that $P_x(q'_1, q'_2)$ depends only on the separation $x = x_2 - x_1$, owing to translational invariance and the centered coordinates in (23). By parity symmetry, we also have $\mathcal{I}(\psi_*, -q'_*) = \mathcal{I}(\psi_*, q'_*)$. For $x = 0$, the two parabolas coincide, and the quantity \mathcal{I} reduces to the expression found in Eq.(16) for the one-point distribution:

$$x = 0 : \quad \mathcal{I}(\psi_*, q'_*) = \Lambda_\alpha (\psi_* + q'^2_*/2)^{\alpha+3/2}.\tag{27}$$

For later use we define the quantities $\mathcal{A}_\nu(x, q'_*)$ and $\mathcal{R}_\nu(x)$,

$$\nu > -1, \quad x \geq 0 : \quad \mathcal{A}_\nu(x, q'_*) = \int_0^\infty d\psi_* \psi_*^\nu e^{-\mathcal{I}(\psi_*, q'_*)}, \quad \mathcal{R}_\nu(x) = \int_{-\infty}^\infty dq'_* \mathcal{A}_\nu(x, q'_*),\tag{28}$$

which for $x = 0$ give

$$\mathcal{R}_\nu(0) = \frac{2\sqrt{2\pi}\Gamma(\nu+1)}{(2\alpha+3)\Gamma(\nu+3/2)} \Gamma\left(\frac{2\nu+3}{2\alpha+3}\right) \Lambda_\alpha^{-(2\nu+3)/(2\alpha+3)},\tag{29}$$

$$\mathcal{R}'_\nu(0) = -\frac{\sqrt{2\pi}\Gamma(\alpha+\nu+3)\Gamma\left(\frac{2\alpha+2\nu+5}{2\alpha+3}\right)}{(\alpha+1)(\alpha+3/2)(\nu+1)\Gamma(\alpha+\nu+5/2)} \Lambda_\alpha^{-(2\alpha+2\nu+5)/(2\alpha+3)},\tag{30}$$

and for large separations,

$$x \gg 1 : \quad \mathcal{R}_\nu(x) \sim x^{-(\nu+3/2)(2\alpha+1)} e^{-\Lambda_\alpha 2^{-3\alpha-7/2} x^{2\alpha+3}}.\tag{31}$$

B. Void probabilities

1. Probability of an empty interval

The overdensity within the Eulerian interval $[x_1, x_2]$ is defined by

$$\rho_{x_1, x_2} = \frac{q_2 - q_1}{x_2 - x_1} \geq 0,\tag{32}$$

where the density has been rescaled by the mean density ρ_0 , though we retain the simpler notation ρ in the following. If the two parabolas share the same contact point, $q_1 = q_2 = q_*$, then the density vanishes, $\rho = 0$, and the interval $[x_1, x_2]$ contains no matter. From Eq.(24), the probability that the interval is empty is therefore

$$P_{\text{void}}(x) = \mathcal{R}_\alpha(x),\tag{33}$$

where the function $\mathcal{R}_\alpha(x)$ was introduced in Eq.(28). Using the results (29) and (31), we obtain

$$P_{\text{void}}(0) = 1 \quad \text{and for} \quad x \gg 1 : \quad P_{\text{void}}(x) \sim x^{-(\alpha+3/2)(2\alpha+1)} e^{-\Lambda_\alpha 2^{-3\alpha-7/2} x^{2\alpha+3}}.\tag{34}$$

Thus, the void probability approaches unity as $x \rightarrow 0$ and decreases as a stretched exponential for large intervals. The result $P_{\text{void}}(0) = 1$ reflects the fact that voids fill the entire Eulerian space, with matter concentrated in Dirac-like density peaks of zero width. The void probability $P_{\text{void}}(x)$ is shown in Fig. 3. it displays a monotonic decrease from unity for $x > 0$ with stretched-exponential tails that agree with Eq.(34).

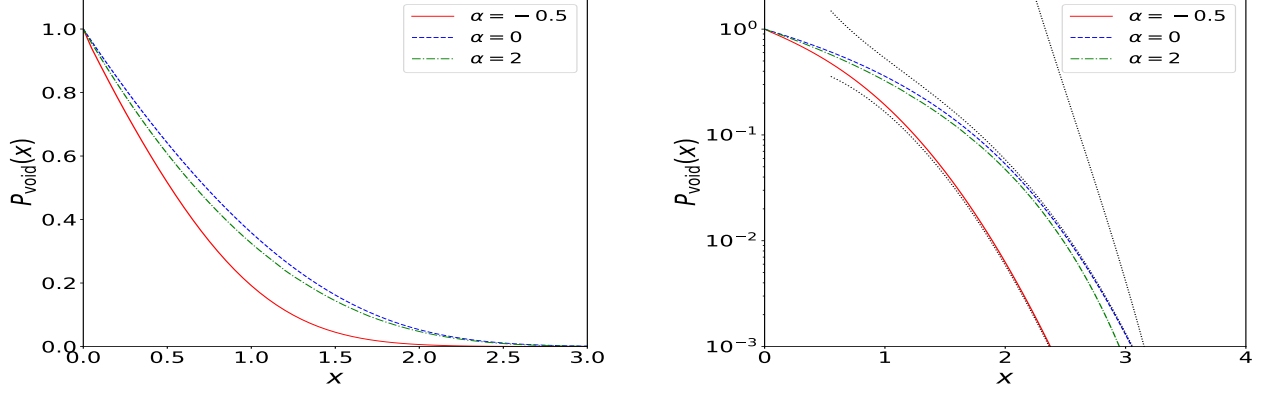


Figure 3. Void probability $P_{\text{void}}(x)$ from Eq.(33), for the cases $\alpha = -1/2, 0$, and 2 , as in Fig. 2. The dotted lines in the right panel are the asymptotic stretched exponentials (34).

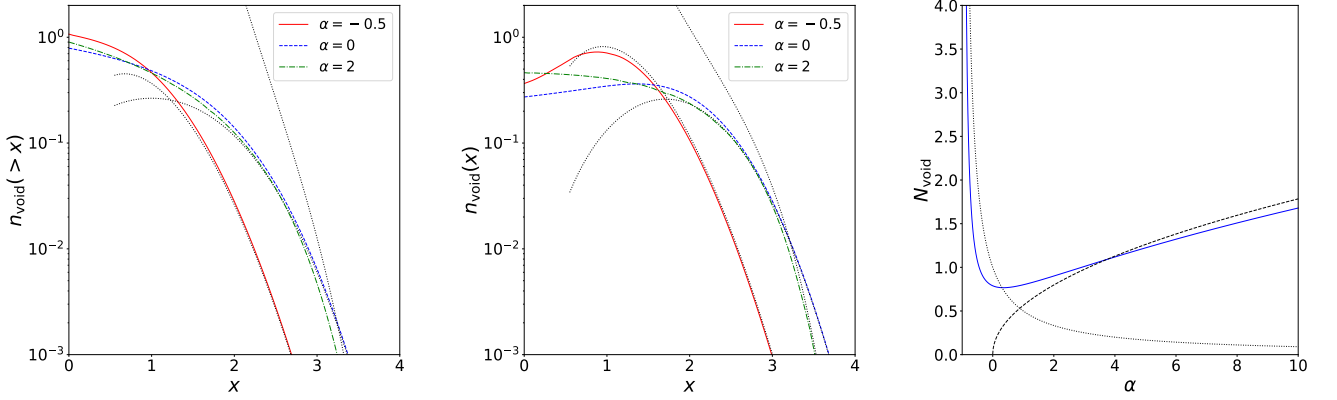


Figure 4. *Left panel:* cumulative void multiplicity function $n_{\text{void}}(> x)$ from Eq.(35). *Middle panel:* void multiplicity function $n_{\text{void}}(x)$ from Eq.(35). *Right panel:* number density of voids N_{void} as a function of α (solid blue line). In the left and middle panels, the dotted lines are the stretched exponentials associated with Eq.(36). In the right panel the dotted and dashed lines are the asymptotic regimes (38).

2. Multiplicity function of voids and distance between shocks

Let $n_{\text{void}}(x)dx$ denote the number of voids per unit length with sizes in the interval $[x, x + dx]$. It is related to the void probability $P_{\text{void}}(x)$ by

$$P_{\text{void}}(x) = \int_x^\infty dx' n_{\text{void}}(x') (x' - x), \quad \text{whence} \quad n_{\text{void}}(> x) = -\frac{dP_{\text{void}}}{dx} = -\mathcal{R}'_\alpha(x), \quad n_{\text{void}}(x) = \frac{d^2 P_{\text{void}}}{dx^2} = \mathcal{R}''_\alpha(x). \quad (35)$$

Using the asymptotic expression (31) and $P_{\text{void}}(0) = 1$, we obtain

$$x \gg 1: \quad n_{\text{void}}(x) \sim x^{-2\alpha^2+5/2} e^{-\Lambda_\alpha 2^{-3\alpha-7/2} x^{2\alpha+3}}, \quad \text{and} \quad \int_0^\infty dx n_{\text{void}}(x) x = 1, \quad (36)$$

which again reflects the fact that voids occupy the entire Eulerian space. From Eq.(30) the number of voids N_{void} per unit length is

$$N_{\text{void}} = n_{\text{void}}(> 0) = -\mathcal{R}'_\alpha(0) = \frac{\sqrt{2\pi}\Gamma(2\alpha+3)\Gamma\left(\frac{4\alpha+5}{2\alpha+3}\right)}{(\alpha+1)^2(\alpha+3/2)\Gamma(2\alpha+5/2)} \Lambda_\alpha^{-(4\alpha+5)/(2\alpha+3)}. \quad (37)$$

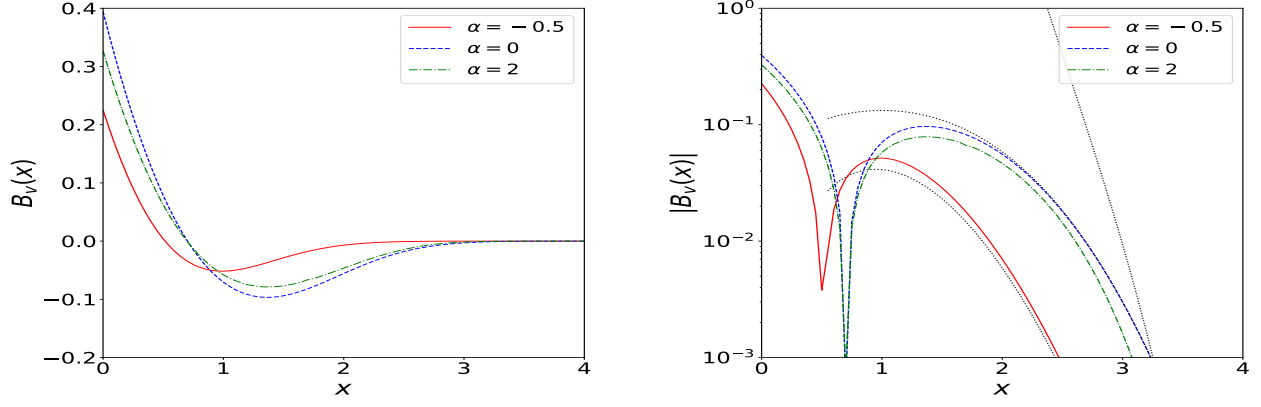


Figure 5. Velocity correlation $B_v(x)$ for the cases $\alpha = -0.5, 0$, and 2 . In the right panel the dotted lines are the asymptotic stretched exponentials (44).

Its limiting behaviors are

$$\alpha \rightarrow -1: N_{\text{void}} \sim \frac{1}{\alpha + 1}, \quad \text{and for } \alpha \rightarrow \infty: N_{\text{void}} \sim \sqrt{\alpha/\pi}, \quad (38)$$

so that the number of voids per unit length diverges in both limits $\alpha \rightarrow -1$ and $\alpha \rightarrow \infty$. The mean void size is given by

$$\langle x \rangle_{\text{void}} = \frac{\int_0^\infty dx n_{\text{void}}(x) x}{\int_0^\infty dx n_{\text{void}}(x)} = \frac{1}{N_{\text{void}}}, \quad (39)$$

and therefore vanishes as $\alpha \rightarrow -1$ and $\alpha \rightarrow \infty$. Since the system consists of a series of shocks separated by voids, the void multiplicity function $n_{\text{void}}(x)$ also provides the probability distribution $P(x_s)$ of the distance x_s between adjacent shocks,

$$P(x_s) = \frac{n_{\text{void}}(x_s)}{N_{\text{void}}} = -\frac{\mathcal{R}_\alpha''(x_s)}{\mathcal{R}_\alpha'(0)}. \quad (40)$$

The void multiplicity functions $n_{\text{void}}(> x)$ and $n_{\text{void}}(x)$ are shown in the left and central panels of Fig. 4, and the mean number of voids per unit length is displayed in the right panel. The void multiplicity function $n_{\text{void}}(x)$ is somewhat more sensitive to α than $P_{\text{void}}(x)$ as the sign of its slope at the origin can change sign with the value of α .

C. Two-point velocity correlation and energy power spectrum

Using $v_1 = x_1 - q_1 = -q'_1 - x/2$, $v_2 = x_2 - q_2 = -q'_2 + x/2$, and the expression (24) for the joint distribution of q'_1 and q'_2 , we obtain the velocity correlation between two points separated by $x = x_2 - x_1 \geq 0$,

$$B_v(x) \equiv \langle v_1 v_2 \rangle_x = \int_{-\infty}^{\infty} dq'_\star \int_0^\infty d\psi_\star \left[\psi_\star^\alpha \left(q'^2_\star - \frac{x^2}{4} \right) - \frac{x}{(\alpha + 1)^2} \psi_\star^{2\alpha+2} \right] e^{-\mathcal{I}(\psi_\star, q'_\star)}, \quad (41)$$

where we have already integrated over q'_1 and q'_2 . Configurations with $\psi_\star \leq 0$ do not contribute, as in this case the parabolic arcs \mathcal{P}_1 and \mathcal{P}_2 in the upper half-plane are disjoint. Then, the integral over either symmetric arc yields a vanishing mean velocity: the contributions from the two sides of x_1 along \mathcal{P}_1 have identical weights but opposite velocities $v_1 = x_1 - q_1$. As for the Fréchet-type case studied in [26], an integration by parts with respect to ψ_\star shows that (41) can also be written as

$$B_v(x) = \frac{1}{\alpha + 1} \int_{-\infty}^{\infty} dq'_\star \left(x \frac{\partial}{\partial x} - q'_\star \frac{\partial}{\partial q'_\star} \right) \mathcal{A}_{\alpha+1}, \quad (42)$$

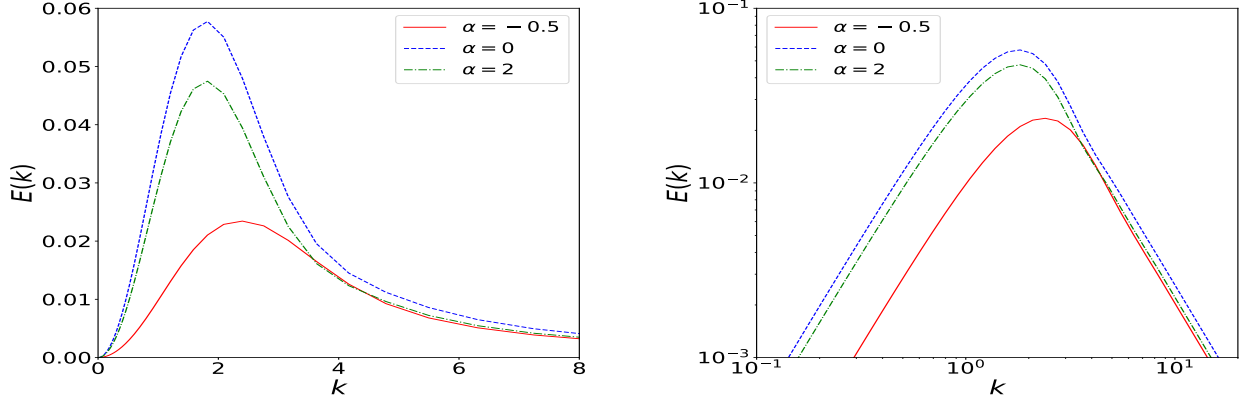


Figure 6. Velocity power spectrum $E(k)$ on linear and logarithmic scales.

where \mathcal{A}_ν is defined in Eq.(28). Performing the integration by parts over q'_* yields

$$x \geq 0: \quad B_v(x) = \frac{1}{\alpha + 1} \frac{d}{dx} [x \mathcal{R}_{\alpha+1}(x)], \quad (43)$$

with \mathcal{R}_ν defined in Eq.(28). By parity, $B_v(-x) = B_v(x) = B_v(|x|)$. This gives the small- and large-scale asymptotic behaviors

$$|x| \ll 1: B_v(x) = \frac{\mathcal{R}_{\alpha+1}(0)}{\alpha + 1} + \frac{2\mathcal{R}'_{\alpha+1}(0)}{\alpha + 1} |x| + \dots, \quad |x| \gg 1: \quad B_v(x) \sim -x^{-2\alpha^2-4\alpha+1/2} e^{-\Lambda_\alpha 2^{-3\alpha-7/2} x^{2\alpha+3}}. \quad (44)$$

The non-analytic $|x|$ term, which carries a negative prefactor, reflects the contribution of shocks. Its linear dependence on $|x|$ corresponds to the probability of encountering at least one shock within an interval of size $|x|$, which decreases linearly following the slope of the complementary void probability $1 - P_{\text{void}}(|x|)$. A shock at position x_s induces a discontinuous decrease in the velocity, $v(x_s^+) - v(x_s^-) < 0$, producing the characteristic sawtooth pattern of Burgers dynamics, illustrated in Fig. 1. This explains the negative coefficient of the $|x|$ term in (44).

The resulting velocity correlation function is shown in Fig. 5. It is positive at small separations, $|x| \lesssim 1$, and it becomes negative at large separations, $|x| \gg 1$, in agreement with the asymptotics (44) and Eq.(29).

The energy spectrum $E(k)$ is the Fourier transform of B_v ,

$$E(k) \equiv \int_{-\infty}^{\infty} \frac{dx}{2\pi} B_v(x) e^{ikx} = \int_0^{\infty} \frac{dx}{\pi} B_v(x) \cos(kx) = \frac{k}{\pi(\alpha + 1)} \int_0^{\infty} dx x \mathcal{R}_{\alpha+1}(x) \sin(kx), \quad (45)$$

where we used $B_v(-x) = B_v(x)$ and Eq.(43), followed by an integration by parts. This implies the low-wavenumber behavior

$$|k| \ll 1: \quad E(k) \simeq \frac{k^2}{\pi(\alpha + 1)} \int_0^{\infty} dx x^2 \mathcal{R}_{\alpha+1}(x) \propto k^2, \quad (46)$$

so that the energy spectrum universally exhibits a quadratic decay at small k . At large wavenumbers, the non-analytic $|x|$ term in $B_v(x)$ produces the universal k^{-2} tail

$$|k| \gg 1: \quad E(k) \simeq \sqrt{\frac{2}{\pi}} \frac{8\Gamma(2\alpha + 2)\Gamma\left(\frac{4\alpha+7}{2\alpha+3}\right)}{(\alpha + 1)(\alpha + 2)\Gamma(2\alpha + 7/2)} \Lambda_\alpha^{-(4\alpha+7)/(2\alpha+3)} k^{-2}. \quad (47)$$

The resulting energy spectrum is shown in Fig. 6. It remains positive for all wavenumbers and matches the asymptotic behaviors (46)-(47).

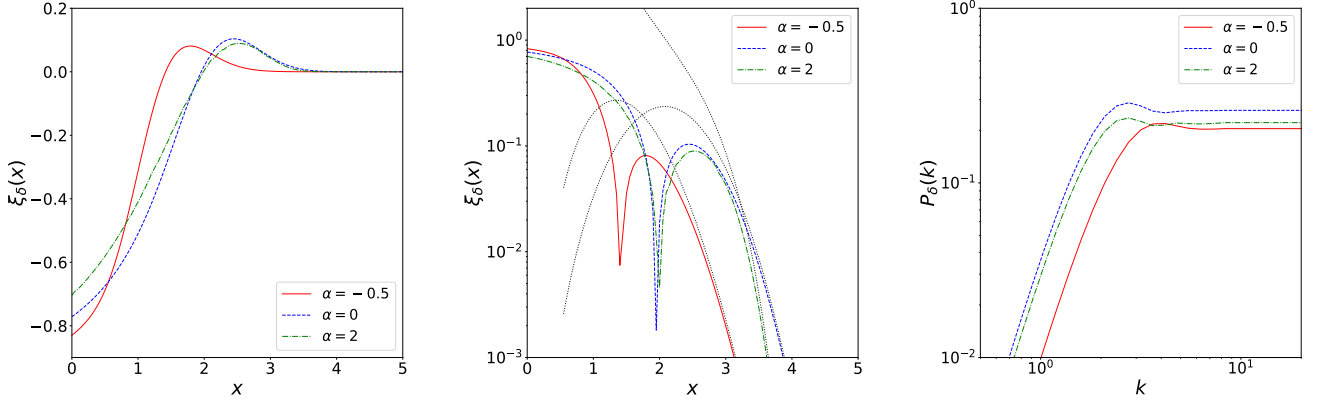


Figure 7. *Left and middle panels:* density correlation function $\xi_\delta^\neq(x)$ on linear and logarithmic scales for $x > 0$. *Right panel:* density power spectrum $P_\delta(k)$.

D. Density correlation and power spectrum

The conservation of matter, encoded in the continuity equation, implies that the density field $\rho(x)$ (normalized by the mean density of the system) and the density contrast $\delta = \rho - 1$ are given by

$$\rho(x) = \frac{dq}{dx}, \quad \delta(x) = -\frac{dv}{dx}, \quad \text{and} \quad \langle \rho \rangle = 1, \quad \langle \delta \rangle = 0, \quad (48)$$

in terms of the Eulerian map $q(x)$ and the velocity field $v(x)$, where we used $v(x) = x - q(x)$. Defining the two-point density correlation function $\xi_\delta(x) = \langle \delta(x_1)\delta(x_1 + x) \rangle$ and the associated power spectrum $P_\delta(k)$, we obtain

$$\xi_\delta(x) = -B_v''(x), \quad P_\delta(k) = k^2 E(k), \quad (49)$$

where $B_v(x)$ and $E(k)$ denote the velocity correlation function and the energy spectrum introduced in Section IV C. Using the results in Eqs.(43) and (44), we find

$$\xi_\delta(x) = \xi_0 \delta_D(x) + \xi_\delta^\neq(x), \quad \text{with for } x > 0: \xi_\delta^\neq(x) = -\frac{1}{\alpha + 1} \frac{d^3}{dx^3} [x \mathcal{R}_{\alpha+1}(x)], \quad (50)$$

$$\xi_0 = -\frac{4}{\alpha + 1} \mathcal{R}'_{\alpha+1}(0) = \frac{16\sqrt{2\pi}\Gamma(2\alpha + 2)\Gamma\left(\frac{4\alpha+7}{2\alpha+3}\right)}{(\alpha + 1)(\alpha + 2)\Gamma(2\alpha + 7/2)} \Lambda_\alpha^{-(4\alpha+7)/(2\alpha+3)} > 0, \quad (51)$$

where the Dirac contribution $\xi_0 \delta_D(x)$ arises from the absolute-value term in Eq.(44) and accounts for the presence of shocks, while $\xi_\delta^\neq(x)$ is a finite and even function. These relations provide closed-form expressions and asymptotic behaviors of $\xi(x)$ and $P_\delta(k)$. In particular,

$$|x| \gg 1: \xi_\delta(x) \sim x^{-2\alpha^2+9/2} e^{-\Lambda_\alpha 2^{-3\alpha-7/2} x^{2\alpha+3}}, \quad (52)$$

$$|k| \ll 1: P_\delta(k) \propto k^4, \quad |k| \gg 1: P_\delta(k) \simeq \sqrt{\frac{2}{\pi}} \frac{8\Gamma(2\alpha + 2)\Gamma\left(\frac{4\alpha+7}{2\alpha+3}\right)}{(\alpha + 1)(\alpha + 2)\Gamma(2\alpha + 7/2)} \Lambda_\alpha^{-(4\alpha+7)/(2\alpha+3)}. \quad (53)$$

Figure 7 shows the density correlation function and the associated power spectrum. The density correlation is negative at small separations, $x \ll 1$, reflecting the depletion of mass in the Eulerian region surrounding shocks. It also becomes negative at large separation. Thus, although the initial conditions generated by the Poisson point process are completely uncorrelated, the nonlinear Burgers dynamics generate nontrivial correlations on large scales, which nevertheless decay as a stretched exponential. Similar to the velocity power spectrum, the density spectrum exhibits only a weak dependence on α , as it follows the universal large-scale k^4 behavior and approaches a constant at high wavenumbers, consistent with Eq.(53).

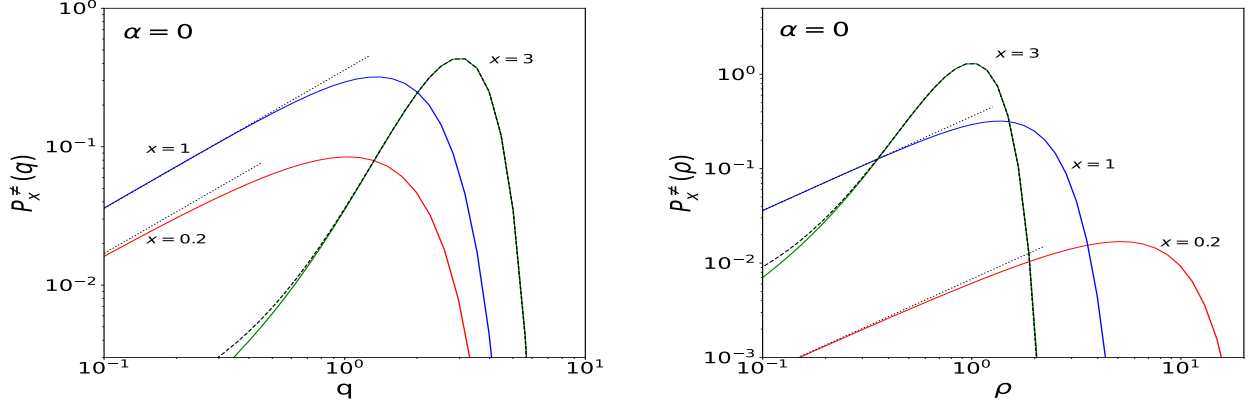


Figure 8. *Left panel:* probability distribution $P_x^\#(q)$ for the case $\alpha = 0$, for the three scales $x = 0.2, 1$, and 3 . The black dotted lines are the small- q linear asymptote (58) and the black dashed line for $x = 3$ is the large-separation asymptote (59). *Right panel:* probability distribution $P_x^\#(\rho)$ for the same cases.

E. Lagrangian increment

We now consider the distribution of the Lagrangian increment $q = q_2 - q_1 = q'_2 - q'_1$ associated with the Eulerian interval $[x_1, x_2]$. It is defined by

$$x = x_2 - x_1 \geq 0, \quad q = q_2 - q_1 \geq 0: \quad P_x(q) = \int_{-\infty}^{\infty} dq'_1 dq'_2 P_x(q'_1, q'_2) \delta_D(q'_2 - q'_1 - q). \quad (54)$$

From Eq.(24), this distribution contains a Dirac contribution—corresponding to the case $q_1 = q_2 = q_*$ —and a regular part,

$$P_x(q) = P_{\text{void}}(x) \delta_D(q) + P_x^\#(q), \quad (55)$$

with

$$P_x^\#(q) = x \int_{-\infty}^{\infty} dq'_* \int_{\psi_{\min}(q'_*)}^{\infty} d\psi_* e^{-\mathcal{I}(\psi_*, q'_*)} \int_{q'_* - q/2}^{q'_* + q/2} dq' \psi_-(q' - q/2)^\alpha \psi_+(q' + q/2)^\alpha. \quad (56)$$

Throughout the paper, we adopt the convention $\int_0^\infty dq \delta_D(q) = 1$, i.e., the Dirac distribution contributes unit mass when integrated over $q \geq 0$. The Dirac component is fully determined by the void probability studied in Section IV B; therefore, in this section we focus on the regular part $P_x^\#(q)$. The total weight of this regular contribution decreases linearly with x at small separations, since $P_{\text{void}} \rightarrow 1$, and satisfies

$$x \rightarrow 0: \quad \int_0^\infty dq P_x^\#(q) = 1 - P_{\text{void}}(x) = N_{\text{void}} x + \dots, \quad x \rightarrow \infty: \quad \int_0^\infty dq P_x^\#(q) \rightarrow 1. \quad (57)$$

Using $q'_2 - q'_1 = x + \frac{\partial \psi_-}{\partial q'_1} - \frac{\partial \psi_+}{\partial q'_2}$ and integration by parts, one can verify that the first moment obeys $\langle q \rangle_x = x$.

From (56), we obtain the small- q linear behavior at fixed x ,

$$q \rightarrow 0: \quad P_x^\#(q) = \mathcal{R}_{2\alpha}(x) x q. \quad (58)$$

For large x and q at fixed $|q - x|$, we obtain

$$x \rightarrow \infty, \quad q \rightarrow \infty, \quad |q - x| \sim 1: \quad P_x^\#(q) \simeq f_\infty^\#(|q - x|) \quad \text{with} \quad f_\infty^\#(q) = \int_{-\infty}^{\infty} dq' P_0(q' + q/2) P_0(q' - q/2), \quad (59)$$

where P_0 is the one-point distribution (16). This is the large-separation limit $x \gg 1$, where the statistics at x_1 and x_2 become independent, as Eq.(59) also reads $P_x^\#(q) \simeq \int_{-\infty}^{\infty} dq_1 dq_2 \delta_D(q_2 - q_1 - q) P_0(q_1 - x_1) P_0(q_2 - x_2)$. For small separations x at fixed q , we obtain

$$x \rightarrow 0: \quad P_x^\#(q) \simeq x n_{\text{shock}}(q) \quad (60)$$

with

$$n_{\text{shock}}(q) = q \int_{q^2/8}^{\infty} dc e^{-\Lambda_\alpha c^{\alpha+3/2}} \int_{q/2-\sqrt{2c}}^{-q/2+\sqrt{2c}} dq' [c - (q' - q/2)^2/2]^\alpha [c - (q' + q/2)^2/2]^\alpha. \quad (61)$$

We will show in Section **VIC** that $n_{\text{shock}}(q)$ is precisely the shock mass function. Thus, in the limit $x \rightarrow 0$, the distribution $P_x(q)$ is governed by the probability of finding either zero shock (captured by $P_{\text{void}}(x) \delta_D(q)$) or one shock (captured by $n_{\text{shock}}(q)$). This reflects the fact that all the matter is contained within discrete shocks. The small- x factorization (60) is consistent with the normalization $\langle q \rangle_x = x$, using Eq.(76) below, which states that all matter is contained within shocks.

The left panel in Fig. 8 shows the regular part $P_x^\neq(q)$ for the case $\alpha = 0$. At large separations $x \gg 1$, the regular component carries almost the full probability mass and the distribution becomes sharply peaked around its mean $\langle q \rangle = x$, the approximation (59) becoming increasingly accurate near the peak and over an expanding range. Since the typical displacement of fluid elements is set by the scale $L(t)$ of Eq.(13), on scales much larger than $L(t)$ the system remains nearly static, implying $x/q \rightarrow 1$.

On small scale $x \ll 1$, the total weight of $P_x^\neq(q)$ decreases linearly with x as in (57), while the peak remains at $q \sim 1$. This reflects the normalization of the full distribution to unity and $\langle q \rangle = x$. The peak position is therefore independent of x and instead set by the characteristic displacement scale $L(t)$, corresponding to $|x - q| \sim 1$ in the rescaled units (10). Thus, as shown in Eq.(60), for $x \ll 1$ the regular part converges toward the fixed shape $n_{\text{shock}}(q)$, with an amplitude proportional to x .

Finally, the mean density ρ within the Eulerian interval $[x_1, x_2]$ of length x is

$$\rho = \frac{q_2 - q_1}{x_2 - x_1} = \frac{q}{x}, \quad \text{and} \quad P_x(\rho) = P_{\text{void}}(x) \delta_D(\rho) + P_x^\neq(\rho) \quad \text{with} \quad P_x^\neq(\rho) = x P_x^\neq(q), \quad (62)$$

where $q = q_2 - q_1$ is the Lagrangian increment as in Section **IV E**. The right panel of Fig. 8 shows the regular component $P_x^\neq(\rho)$ for the case $\alpha = 0$. We again clearly see the linear decrease with x of the total weight of the regular component $P_x^\neq(\rho)$, but the peak now shifts toward high density contrasts, $\rho \sim 1/x$. This trend reflects the increasing inhomogeneity of the system on small Eulerian scales, arising from the alternating sequence of shocks and voids. At large separation, by contrast, the system appears progressively more homogeneous, and the distribution becomes increasingly concentrated around the mean density.

V. HIGHER-ORDER DISTRIBUTIONS

We now turn to higher-order distributions, for which explicit expressions can also be derived, see, for example [30] for the Gaussian case and [26] for Fréchet-type Poisson cases. As for the two-point distribution (21), the analysis simplifies when we consider together the two variables (q_i, c_i) associated with an Eulerian point x_i . Owing to the uncorrelated nature of the underlying initial Poisson point process and to the ordering $q_1 \leq q_2 \leq \dots \leq q_n$ for $x_1 < x_2 < \dots < x_n$, the n -point distribution can be written as

$$x_1 < x_2 < \dots < x_n : \quad P_{x_1, \dots, x_n}(q_1, c_1; \dots; q_n, c_n) = P_{x_1}(q_1, c_1) \prod_{i=2}^n P_{x_i, x_{i-1}}(q_i, c_i | q_{i-1}, c_{i-1}), \quad (63)$$

where $P_{x_1}(q_1, c_1) = P_0(q_1 - x_1, c_1)$ is the one-point distribution obtained in Section **III**, and $P_{x_i, x_{i-1}}(q_i, c_i | q_{i-1}, c_{i-1})$ is the conditional probability

$$P_{x_2, x_1}(q_2, c_2 | q_1, c_1) = [\delta_D(q_2 - q_1) \delta_D(c_2 - c_{12}) + \theta(q_2 > q_{12}) \theta(c_2 < c_{12}) \lambda(c_2 - (q_2 - x_2)^2/2)] \\ \times e^{-\int_{q_{12}}^{\infty} dq \int_{c_1 - (q - x_1)^2/2}^{c_2 - (q - x_2)^2/2} d\psi \lambda(\psi)}. \quad (64)$$

One may verify that this expression reduces to Eq.(21) for the two-point distribution. Here c_{12} denotes the height of the parabola \mathcal{P}_{x_2, c_2} that intersects the previous parabola \mathcal{P}_{x_1, c_1} at the position q_1 . For arbitrary height c_2 , we changed notation from q_* to q_{12} for the intersection of both parabolas,

$$c_{12} = c_1 + \frac{(q_1 - x_2)^2 - (q_1 - x_1)^2}{2}, \quad q_{12}(c_2) = \frac{x_1 + x_2}{2} + \frac{c_1 - c_2}{x_2 - x_1}. \quad (65)$$

The normalization is easily checked, $\int dc_2 dq_2 P_{x_2, x_1}(q_2, c_2 | q_1, c_1) = 1$.

The factorization (63) holds because, for example in the three-point case, one can verify that $q_{13} \geq q_{12}$. Thus, the intersection of \mathcal{P}_1 and \mathcal{P}_3 is irrelevant: it always occurs in a region where \mathcal{P}_2 already dominates \mathcal{P}_1 , i.e., $\mathcal{P}_2 \geq \mathcal{P}_1$. Consequently, the parabolic arcs follow the same ordering $(\mathcal{P}_1, \dots, \mathcal{P}_n)$ as the Eulerian points (x_1, x_2, \dots, x_n) over the domains $-\infty < q_{12} \leq q_{23} \leq \dots \leq q_{n-1,n} < \infty$. Therefore, when adding a new point x_n in the n -point distribution (63), it is sufficient to consider only the preceding parabola $\mathcal{P}_{x_{n-1}, c_{n-1}}$ and its contact point q_{n-1} . As in the two-point case (21), one must distinguish whether the new contact point q_n coincide with q_{n-1} —the first term in Eq.(64), which prevents assigning a double Poisson weight to the same contact point—or whether it lies to the right, corresponding to the second term. Finally, the exponential factor accounts for the requirement that the region in the (q, ψ) plane above the preceding parabola \mathcal{P}_{n-1} and below the new parabola \mathcal{P}_n contains no Poisson points.

VI. LAGRANGIAN DISTRIBUTIONS OR PARTICLE DISPLACEMENTS

In this Section, we turn to Lagrangian statistics, focusing on the distribution of Eulerian positions x for particles with prescribed Lagrangian coordinates q . Equivalently, this corresponds to the statistics of the displacements $x - q$, where each particle is labeled by its initial positions q .

A. One-point Lagrangian distribution

Because particles do not cross, the Lagrangian probability $P_q(\geq x)$ that the particle labeled by q lies to the right of position x is equal to the Eulerian probability $P_x(\leq q)$ that the Lagrangian coordinate $q(x)$ of the particle located at x is less than or equal to q . Differentiating this relation with respect to x , and using the identity $P_x(q) = P_0(q - x)$ derived in Section III, yields

$$P_q(\geq x) = P_x(\leq q) \quad \text{and} \quad P_q(x) = P_0(x - q) = P_x(q). \quad (66)$$

Thus, the one-point Lagrangian and Eulerian distributions are identical, and all properties of $P_q(x)$ follow directly from the results obtained in Section III.

B. Two-point Lagrangian distribution

As in the case of one-point statistics, the two-point Lagrangian and Eulerian probabilities are related by

$$P_{q_1, q_2}(\geq x_1, \leq x_2) = P_{x_1, x_2}(\leq q_1, \geq q_2), \quad P_{q_1, q_2}(x_1, x_2) = -\frac{\partial^2}{\partial x_1 \partial x_2} \int_{-\infty}^{q_1} dq_1'' \int_{q_2}^{\infty} dq_2'' P_{x_1, x_2}(q_1'', q_2''). \quad (67)$$

Using statistical homogeneity, which implies $P_{x_1, x_2}(q_1, q_2) = P_x(q_1 - \bar{x}, q_2 - \bar{x})$ as in Eq.(24), and changing variables from (x_1, x_2) to (x, \bar{x}) , we obtain

$$P_{q_1, q_2}(x_1, x_2) = \left(\frac{\partial^2}{\partial x^2} - \frac{1}{4} \frac{\partial^2}{\partial \bar{x}^2} \right) \int_{-\infty}^0 dq_1' \int_q^{\infty} dq_2' P_x(q_1' + q_1 - \bar{x}, q_2' + q_1 - \bar{x}), \quad (68)$$

where $q = q_2 - q_1$. As in Section IV E, we focus on the probability distribution of the Eulerian increment x ,

$$P_q(x) = \int dx_1 dx_2 P_{q_1, q_2}(x_1, x_2) \delta_D(x_2 - x_1 - x). \quad (69)$$

Changing variables again from (x_1, x_2) to (x, \bar{x}) and making use of (54), we obtain the relation between the distributions of Lagrangian and Eulerian increments,

$$q > 0 : \quad P_q(x) = P_{\text{shock}}(q) \delta_D(x) + P_q^{\neq}(x) \quad \text{with} \quad P_q^{\neq}(x) = \frac{\partial^2}{\partial x^2} \int_q^{\infty} dq' P_x^{\neq}(q')(q' - q), \quad (70)$$

where the Dirac term in Eq.(55) does not contribute for $q > 0$, and we have explicitly added the term $P_{\text{shock}}(q)\delta_D(x)$, which corresponds to the probability that the entire interval $[q_1, q_2]$ lies within a single shock. The latter contribution

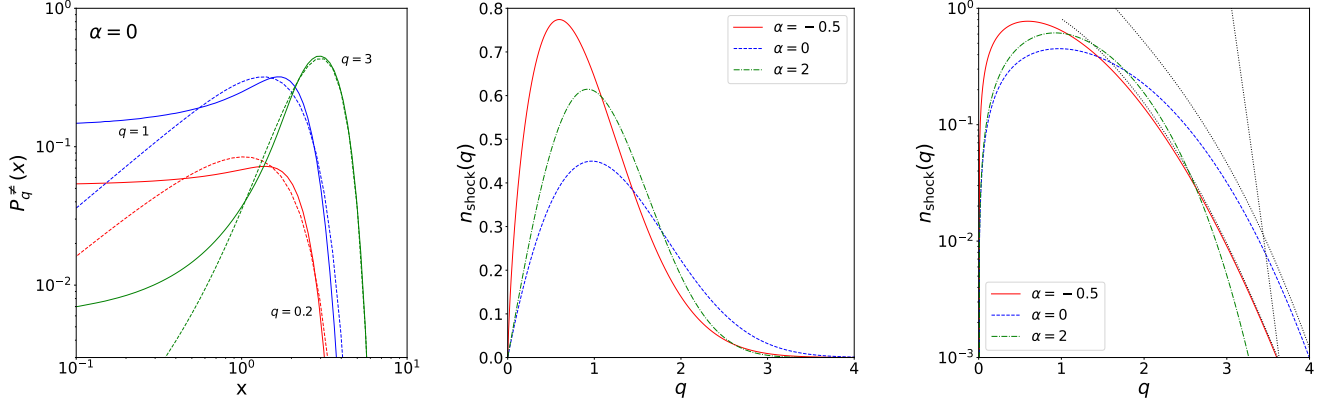


Figure 9. *Left panel:* probability distribution $P_q^\#(x)$ of the Eulerian increment x , for the case $\alpha = 0$ and the three scales $q = 0.2, 1$, and 3 , as in Fig. 8. *Middle and right panels:* shock multiplicity function from Eq.(61) for the cases $\alpha = -0.5, 0$, and 2 .

is not included in the regular term $P_q^\#(x)$. Writing the integral q as $\int_q^\infty = \int_0^\infty - \int_0^q$ and using Eqs.(55) together with $\langle q \rangle_x = x$, we can rewrite

$$P_q^\#(x) = q n_{\text{void}}(x) + \frac{\partial^2}{\partial x^2} \int_0^q dq' P_x^\#(q')(q - q'), \quad \text{whence } \langle x \rangle_q = q, \quad (71)$$

where the equality for the mean follows from integrations by parts and the result $P_{\text{void}}(0) = 1$ from Eq.(34). This confirms that the system exhibits no net expansion or contraction: particle displacements occur on the scale $L(t)$ introduced in Eq.(13), and therefore $x/q \rightarrow 1$ for $q \rightarrow \infty$. Consequently, $\langle x \rangle_q = q$ for any Lagrangian interval.

For small Lagrangian separations at fixed x we find

$$q \rightarrow 0: \quad P_q^\#(x) \simeq q n_{\text{void}}(x). \quad (72)$$

This factorized form is analogous to Eq.(60) for the Eulerian distribution $P_x^\#(q)$ at small x . It shows that, for small Lagrangian mass intervals $q \rightarrow 0$, the Eulerian distance distribution is determined, to order q , by the probability of being fully contained within a shock (contributing the term $P_{\text{shock}}(q) \delta_D(x)$) or by containing a single void (described by the void multiplicity function $n_{\text{void}}(x)$). This reflects the discreteness of voids in Lagrangian space and the fact that they occupy all of the Eulerian volume. The normalization $\langle x \rangle_q = q$, together with Eq.(36), is fully consistent with the small- q behavior in Eq.(72).

At large scales, the Eulerian distribution takes the form $P_x^\#(q) \simeq f_\infty^\#(|q - x|)$, as given by Eq.(59). Substituting this into Eq.(70) yields

$$q \rightarrow \infty, \quad x \rightarrow \infty, \quad |x - q| \sim 1: \quad P_q^\#(x) \simeq f_\infty^\#(|x - q|) \simeq P_x^\#(q). \quad (73)$$

As expected, the distribution is sharply peaked at the mean $\langle x \rangle_q = q$, with a width set by the characteristic displacement scale of the particles.

The left panel of Fig. 9 shows the distribution $P_q^\#(x)$. As in the Eulerian case displayed in Fig. 8, the weight of this regular component decreases linearly with q on small scales, in agreement with Eq.(72), while its characteristic width—visible through the sharp cutoff—remains of order unity and is set by the typical void size. The main difference relative to the Eulerian distribution is that $P_q^\#(x)$ does not decrease linearly with x at small separations; instead it approaches a finite constant as $x \rightarrow 0$. At large separations, the distribution becomes again increasingly sharply peaked around its mean $\langle x \rangle_q = q$, and Eulerian and Lagrangian statistics converge, with $P_q^\#(x) \simeq P_x^\#(q)$.

C. Multiplicity function of shocks

The probability $P_{\text{shock}}(q)$ that a Lagrangian interval of size q is entirely contained within a single shock follows from the normalization of the full distribution $P_q(x)$ in Eq.(70):

$$P_{\text{shock}}(q) = 1 - \int_0^\infty dx P_q^\#(x) = 1 - N_{\text{void}} q + \frac{\partial}{\partial x} \bigg|_{x=0} \int_0^q dq' P_x^\#(q')(q - q'), \quad (74)$$

where we have used Eq.(71). The quantity $P_{\text{shock}}(q)$ is also related to the shock multiplicity function $n_{\text{shock}}(q)dq$, defined as the number of shocks per unit length with Lagrangian mass in the interval $[q, q + dq]$, through

$$P_{\text{shock}}(q) = \int_q^\infty dq' n_{\text{shock}}(q') (q' - q), \quad \text{whence } n_{\text{shock}}(q) = \frac{d^2 P_{\text{shock}}}{dq^2} = \frac{\partial}{\partial x} \Big|_{x=0} P_x^\neq(q). \quad (75)$$

This immediately yields

$$\int_0^\infty dq n_{\text{shock}}(q) q = P_{\text{shock}}(0) = 1, \quad (76)$$

which expresses the fact that all matter is bound within shocks. Using the small- x behavior of $P_x^\neq(q)$ from Eq.(60), one recovers the expression for $n_{\text{shock}}(q)$ given in Eq.(61). This provides, in particular, the small- and large-mass asymptotic falloffs

$$q \rightarrow 0 : n_{\text{shock}}(q) \simeq \mathcal{R}_{2\alpha}(0) q, \quad \text{and for } q \rightarrow \infty : n_{\text{shock}}(q) \sim q^{-2(\alpha+1)(2\alpha+1)} e^{-\Lambda_\alpha 2^{-3\alpha-9/2} q^{2\alpha+3}}. \quad (77)$$

The middle and right panels in Fig. 9 show the shock multiplicity functions. We recover the asymptotic regimes (77).

VII. CONCLUSION

In this paper, we have presented a detailed analytical characterization of the statistical properties of one-dimensional Burgers dynamics for a class of initial conditions generated by a Poisson point process with a power-law intensity of exponent $\alpha > -1$. This family leads to Weibull-type statistics, featuring stretched-exponential tails. It is therefore complementary to the case of Fréchet-type statistics with power-law tails, investigated in the companion paper [26], which arises when the Poisson intensity follows a power-law with exponent $\alpha < -3/2$. The two cases together provide a unified framework covering the full range of admissible exponents and reveal how the sign of the intensity exponent leads to qualitatively distinct statistical regimes in Burgers turbulence.

Exploiting the geometrical interpretation of the solution in terms of parabolic first-contact points, we obtained exact expressions for a wide class of Eulerian and Lagrangian observables, including one-point and multi-point distributions, shock and void multiplicity functions, and the full probability density of Lagrangian and Eulerian increments. The formalism applies to arbitrary exponent $\alpha > -1$ and it includes, as a limiting case with a proper rescaling, the traditional case of Gaussian initial conditions without large-scale power [9].

We established closed-form expressions for the shock mass function and void-size distribution, together with their large-mass and large-size asymptotic behaviors. The derived relations explicitly show how these quantities control the small-scale structure of Eulerian and Lagrangian increments, leading to simple factorized forms in the limits of small intervals. On large scales, we demonstrated that both Eulerian and Lagrangian increment statistics converge to peaked distributions governed by the one-point distribution $P_0(q)$, with widths determined by the characteristic displacement scale $L(t)$.

In addition, the paper presents an exact factorization of the full n -point distributions into a sequence of two-point conditional probabilities. This property follows from the ordered structure of the parabolic envelopes and substantially simplifies the statistical description of the process. The resulting framework provides a unified and fully tractable description of Burgers turbulence for this broad class of initial conditions.

-
- [1] J. M. Burgers, *The Nonlinear Diffusion Equation* (Springer Netherlands, 1974).
 - [2] E. Hopf, The partial differential equation $ut + uux = \mu xx$, *Communications on Pure and Applied Mathematics* **3**, 201 (1950).
 - [3] J. D. Cole, On a quasi-linear parabolic equation occurring in aerodynamics, *Quarterly of Applied Mathematics* **9**, 225 (1951).
 - [4] S. N. Gurbatov, A. I. Saichev, S. N. Gurbatov, and A. I. Saichev, Degeneracy of one-dimensional acoustic turbulence under large Reynolds numbers, *ZhETF* **80**, 689 (1981).
 - [5] G. B. Whitham, *Linear and Nonlinear Waves* (wiley, 1999).
 - [6] U. Frisch and J. Bec, *New trends in turbulence Turbulence: nouveaux aspects* (Springer, Berlin, Heidelberg, 2001) pp. 341–383, [arXiv:0012033 \[nlin\]](#).
 - [7] J. Bec and K. Khanin, Burgers turbulence, *Physics Reports* **447**, 1 (2007).
 - [8] R. H. Kraichnan, Lagrangian-History Statistical Theory for Burgers' Equation, *The Physics of Fluids* **11**, 265 (1968).

- [9] S. Kida, Asymptotic properties of Burgers turbulence, *Journal of Fluid Mechanics* **93**, 337 (1979).
- [10] L. Frachebourg, P. A. Martin, and J. Piasecki, Ballistic aggregation: a solvable model of irreversible many particles dynamics, *Physica A: Statistical Mechanics and its Applications* **279**, 69 (2000).
- [11] P. Valageas, Ballistic aggregation for one-sided Brownian initial velocity, *Physica A: Statistical Mechanics and its Applications* **388**, 1031 (2009).
- [12] S. N. Gurbatov, A. I. Saichev, S. F. Shandarin, S. N. Gurbatov, A. I. Saichev, and S. F. Shandarin, The large-scale structure of the universe in the frame of the model equation of non-linear diffusion, *MNRAS* **236**, 385 (1989).
- [13] S. Gurbatov, A. Malakhov, and A. I. Saichev, *Nonlinear random waves and turbulence in nondispersive media : waves, rays, particles* (Manchester University Press ; Distributed exclusively in the US and Canada by St. Martin's Press, 1991).
- [14] M. Vergassola, B. Dubrulle, U. Frisch, A. Noullez, M. Vergassola, B. Dubrulle, U. Frisch, and A. Noullez, Burgers' equation, Devil's staircases and the mass distribution for large-scale structures., *A&A* **289**, 325 (1994).
- [15] P. Valageas and F. Bernardeau, Density fields and halo mass functions in the geometrical adhesion toy model, *Physical Review D* **83**, 043508 (2011), [arXiv:1009.1974](#).
- [16] Y. B. Zel'dovich, Gravitational instability: An approximate theory for large density perturbations., *A&A* **5**, 84 (1970).
- [17] S. F. Shandarin and Y. B. Zeldovich, The large-scale structure of the universe: Turbulence, intermittency, structures in a self-gravitating medium, *Reviews of Modern Physics* **61**, 185 (1989).
- [18] Z. S. She, E. Aurell, and U. Frisch, The inviscid Burgers equation with initial data of Brownian type, *Communications in Mathematical Physics* **148**, 623 (1992).
- [19] S. N. Gurbatov, S. I. Simdyankin, E. Aurell, U. Frisch, and G. Tóth, On the decay of Burgers turbulence, *Journal of Fluid Mechanics* **344**, 339 (1997), [arXiv:9709002 \[physics\]](#).
- [20] J. Bertoin, The inviscid burgers equation with Brownian initial velocity, *Communications in Mathematical Physics* **193**, 397 (1998).
- [21] P. Valageas, Statistical properties of the burgers equation with brownian initial velocity, *Journal of Statistical Physics* **134**, 589 (2009).
- [22] L. Frachebourg and P. A. Martin, Exact statistical properties of the Burgers equation, *Journal of Fluid Mechanics* **417**, 323 (2000), [arXiv:9905056 \[cond-mat\]](#).
- [23] P. Valageas, Some statistical properties of the Burgers equation with white-noise initial velocity, *Journal of Statistical Physics* **137**, 729 (2009), [arXiv:0903.0956](#).
- [24] S. A. Molchanov, D. Surgailis, and W. A. Woyczynski, The large-scale structure of the universe and quasi-Voronoi tessellation of shock fronts in forced Burgers turbulence in Rd, *Annals of Applied Probability* **7**, 200 (1997).
- [25] T. Gueudré and P. Le Doussal, Statistics of shocks in a toy model with heavy tails, *Physical Review E - Statistical, Nonlinear, and Soft Matter Physics* **89**, 42111 (2014).
- [26] P. Valageas, Burgers dynamics for poisson point process initial conditions, (2025), [arXiv:2511.03647](#).
- [27] D. Bernard and K. G. Gawędzki, Scaling and exotic regimes in decaying Burgers turbulence, *J. Phys. A: Math. Gen* **31**, 8735 (1998).
- [28] M. Bauer and D. Bernard, Sailing the deep blue sea of decaying burgers turbulence, *Journal of Physics A: Mathematical and General* **32**, 5179 (1999).
- [29] S. N. Gurbatov, O. V. Rudenko, and A. I. Saichev, *Waves and Structures in Nonlinear Nondispersive Media*, Nonlinear Physical Science (Springer Berlin Heidelberg, Berlin, Heidelberg, 2011).
- [30] S. A. Molchanov, D. Surgailis, and W. A. Woyczynski, Hyperbolic asymptotics in Burgers' turbulence and extremal processes, *Communications in Mathematical Physics* **168**, 209 (1995).